Chemistry & Biodiversity

WILEY-VCH

CHEMISTRY & BIODIVERSITY

RESEARCH ARTICLE

Chiral Anthranilic Amides as Potential Cholinesterase Inhibitors: Synthesis, Bioactivity Assessment, and Molecular Modeling

Turgay Tunç[1] | Namık Kılınç[2] | Nadir Demirel[3] | Zuhal Alım[3]

[1]Department of Chemistry Engineering and Process, Faculty of Engineering, University of Kırşehir Ahi Evran, Kırşehir, Türkiye | [2]Department of Medical Services and Techniques, Vocational School of Health Services, University of Iğdır, Iğdır, Türkiye | [3]Department of Chemistry, Faculty of Science and Arts, University of Kırşehir Ahi Evran, Kırşehir, Türkiye

Correspondence: Zuhal Alım (zuhal.alim@ahievran.edu.tr)

Received: 19 March 2025 | **Revised:** 1 June 2025 | **Accepted:** 16 June 2025

Funding: This study was funded by Kırşehir Ahi Evran University (Grants FEF.A3.24.006 and MMF.A3.24.002).

Keywords: acetylcholinesterase | butyrylcholinesterase | chiral anthranilic amide | inhibition | molecular docking

ABSTRACT

Inhibitors of acetylcholinesterase (AChE) and butyrylcholinesterase (BChE) are central therapeutic targets for Alzheimer's disease (AD). In this study, novel chiral anthranilic amide derivatives (**5a–5d**, **7a**, and **7b**) were synthesized from chiral amines and were characterized by ^{1}H, ^{13}C NMR, LC–MS, and IR, then inhibitory effect of **5a–5d**, **7a**, and **7b** on AChE/BChE activity was investigated by in vitro inhibition and in silico studies. For AChE, IC_{50} values of **5a–5d**, **7a**, and **7b** were found to be 70, 63.64, 53.85, 36.84, 17.07, and 17.5 nM, respectively. For BChE, IC_{50} values of **5a–5d**, **7a**, and **7b** were found as 46.66 μM, 33.33 μM, 116.6 μM, 233.3 μM, 175 nM and, 116.6 nM, respectively. All compounds had better inhibition effects against AChE than BChE. The enantioselective inhibition was observed in the compounds **5a–5d**. For AChE, the *S*-enantiomers exhibited stronger inhibition than the *R*-enantiomers. However, in the case of BChE, *R*-enantiomers had better inhibition effects. Although molecules **7a** and **7b** had a stronger inhibition effect than molecules **5a–5d** for AChE and BChE, the enantioselectivity was decreased in these molecules. This result was attributed to the spacer group effect in **7a** and **7b**.

1 | Introduction

Acetylcholinesterase (AChE) and butyrylcholinesterase (BChE) are serine hydrolases liable for the termination and regulation of cholinergic signals in the nervous system by catalysing the hydrolysis of the neurotransmitter acetylcholine (ACh) [1–4]. Abnormal concentrations of cholinesterases (ChEs) in the body are associated with many neural pathologies, including Alzheimer's disease (AD) and Parkinson's disease [5, 6]. Over 55 million people around the world are currently affected by dementia, with AD patients making up the majority of these cases [7, 8]. The number of dementia patients is expected to reach 78 million by 2030 [9, 10] and 139 million by 2050 [7]. As a result, ChE inhibitors play a crucial role in improving the quality of life for millions of people impacted by neural diseases, particularly AD, helping to reduce the increasing socioeconomic burden linked to these conditions [11]. By prolonging the residence time of ACh in the synaptic cleft and cholinergic neurotransmission, ChE inhibitors postpone the symptoms of dementia that occur with the corruption of central cholinergic neurons or the deterioration of cholinergic function [12]. Although great efforts have been made to combat AD, only a few medications, including the ChE inhibitors tacrine, donepezil, rivastigmine, and galantamine (the other drugs: *N*-methyl-D-aspartate [NMDA], receptor antagonist

[memantine], amyloid-β scavenger [aducanumab]) have been approved by the US Food and Drug Administration (FDA) for the treatment of AD [10, 13]. Furthermore, the China National Medical Products Administration has granted approval for two AD treatments, Huperzine A and GV-971 [14]. Although these medications can alleviate the symptoms of AD, they are unable to halt the progression of the degenerative process and may lead to significant side effects. As a result, identifying new and effective treatment options for AD has become essential [10]. For this reason, many studies are being carried out to identify new ChE inhibitors. Most of the current drugs approved for the medication of AD are AChE inhibitors, as mentioned above. This suggests that creating new, potent ChE inhibitors with fewer side effects continues to be a promising approach for treating AD. On the other hand, BChE plays an auxiliary role to AChE in regulating ACh levels, and BChE inhibitors are valuable therapeutic targets for the treatment of AD [15]. Recent Studies have identified some selective AChE and BChE inhibitors and dual AChE and BChE inhibitors [16, 17], with studies in this field continuing rapidly.

Anthranilic acid itself effectively binds to various substituents on biological targets due to the presence of free —COOH and —NH_2 groups in their structure and has a remarkable biological profile due to this chemical property [18–21]. Therefore, anthranilic acid is one of the target molecules used in drug design studies aiming to modulate biochemical and metabolic pathways involved in the pathogenesis of many diseases [21–24]. Anthranilic acid derivatives have been the building blocks for the synthesis of various commercial drugs such as fenamates, NSAIDs [20, 25], and many bioactive compounds [21]. Anthranilic acid derivatives have many biological activities such as antiviral [14], antibacterial [26], anti-inflammatory [27], analgesic, antipyretic [21, 22], and insecticide [28, 29]. In addition, anthranilic acid diamides have potential use as P-glycoprotein inhibitors, to keeping drug resistance under control in cancer cells [21, 30]. Furthermore, research has indicated that α-glucosidase inhibitors derived from anthranilic acid will be significant in managing diabetes [31]. The success of anthranilic acid-based compounds in the pharmaceutical field has increased the potential of new anthranilic acid derivatives as a promising candidate for molecules in drug design studies for the treatment of various diseases.

Amide bonds have important classical geometry and planar properties. These structural features provide a useful application in synthetic and medicinal chemistry [32–34]. In addition, chirality is important in drug design studies as chiral drugs exhibit different biological activities [35]. The fact that the enantiomers of some drugs have different pharmacological and toxicological profiles, it has led to the therapeutic ineffectiveness of these drugs or adverse drug reactions, posing an issue with the safety [36–39]. For this reason, it has become important to develop new drug candidates with pure enantiomer structures instead of racemic or nonracemic isomer mixtures in drug design studies [38–40]. In this study, anthranilic diamide molecules (**5a–5d**, **7a**, **7b**) were synthesized using chiral amine and the potential of these molecules as ChE (for both AChE and BChE) inhibitors was investigated. In addition, in vitro inhibition studies were supported by molecular modeling, molecular dynamics (MD), and absorption, distribution, metabolism, and excretion (ADME) analyses. Therefore, the findings obtained from this study will assist in the discovery of new, pure enantiomer ChE inhibitors for the medication of AD.

2 | Results and Discussion

2.1 | Chemistry

To date, many anthranilic amide derivatives have served as an important group of compounds that form the basic framework of many commercial drugs and bioactive compounds with a wide range of biological activities. The presence of functional groups such as —COOH, —NH_2, —$CONH_2$, —$COOCH_3$, and —$NHCOCH_3$ in anthranilic acid derivatives allows these molecules to interact with biological targets, and due to this feature, anthranilic acid derivatives are among the promising candidate molecules in drug design studies for the treatment of various diseases [20, 21], which driving us to design the novel anthranilic amide derivatives. In this study, anthranilic amide structures were created by using chiral amine. Compounds **5a–5d**, **7a**, and **7b** was synthesized as shown in Scheme 1.

Chiral 2-amino-N-(1-phenylethyl) benzamide derivatives **3a** and **3b** were successfully synthesized as key intermediates for the construction of the target compounds. The synthesis was performed via the reaction of commercially available chiral amines (*R*- or *S*-1-phenylethylamine) with isatoic anhydride in either dioxane or DMF, following previously reported procedures [41–43]. These reactions afforded the desired amide products in good overall yields.

The structures of compounds **3a** and **3b** were confirmed by ^{1}H and ^{13}C NMR spectroscopy, as well as LC–MS analysis. In the ^{1}H NMR spectra, characteristic signals were observed at 1.577 ppm for the methyl group (—CH_3), 5.229 ppm for the methine proton (—CH), 5.516 ppm for the amine group (—NH_2), and 6.365 ppm for the amide proton (—CONH). The ^{13}C NMR spectrum showed a distinct signal at 168.73 ppm corresponding to the carbonyl carbon. The LC–MS spectra supported the assigned structures, with peaks corresponding to the calculated molecular weights (MWs).

Subsequent reaction of compounds **3a** and **3b** with nicotinoyl chloride, 2-chloronicotinoyl chloride, and 2,6-pyridine dicarbonyl dichloride yielded the final target compounds **5a–5d**, **7a**, and **7b**. These reactions were carried out in dichloromethane using potassium carbonate as a base and resulted in good yields of the desired products.

^{1}H NMR analysis of compounds **5a–5d** revealed two amide (—CONH) proton signals in each case, indicating the successful incorporation of the acyl moieties. Specifically, the —CONH peaks appeared at 6.94 and 12.80 ppm for **5a**, 6.65 and 11.629 ppm for **5b**, 6.85 and 12.28 ppm for **5c**, and 6.80 and 11.63 ppm for **5d**. These chemical shift variations suggest that the substitution pattern on the pyridine ring, particularly the presence of electron-withdrawing chlorine atoms, influenced the shielding of the amide protons, leading to observable upfield shifts.

In the ^{13}C NMR spectra of compounds **5a–5d**, two distinct carbonyl carbon signals were recorded around 164 and 168 ppm, consistent with the presence of multiple amide functionalities.

LC–MS data for all final products were in good agreement with their expected molecular masses, further confirming their identities. These results demonstrate the efficiency of the synthetic strategy and highlight the structural influence of different pyridine-based acyl groups on the spectroscopic properties of the final compounds. Upon examination of the IR spectra, compounds **5a** and **5c** exhibit amide carbonyl absorption bands at 1679 cm^{-1}, whereas compounds **5b** and **5d** display these bands at 1684 cm^{-1}. All of these compounds show a characteristic —CONH stretching band at 3318 cm^{-1}.

Chirality plays a critical role in drug design, particularly in minimizing adverse or toxic effects associated with racemic mixtures [44–46]. This understanding guided the incorporation of chiral moieties into the molecular framework of our target compounds. In this study, we strategically designed and synthesized a series of chiral amide derivatives to explore the influence of stereochemistry on the structural and potential biological properties of the molecules.

Compounds **5a** and **5c** share the same molecular scaffold but differ in their stereochemistry. Specifically, **5a** was synthesized using *R*-(+)-1-phenylethylamine, isatoic anhydride, and nicotinoyl chloride, whereas **5c** was prepared using the *S*-(−)-enantiomer of 1-phenylethylamine under otherwise identical conditions. A similar stereochemical distinction exists between compounds **5b** and **5d**, both of which were synthesized using 2-chloronicotinoyl chloride in place of nicotinoyl chloride, with **5b** derived from the *R*-enantiomer and **5d** from the *S*-enantiomer of the chiral amine.

In compounds **7a** and **7b**, 2,6-pyridinedicarbonyl dichloride was employed as a diacylating agent to introduce a rigid spacer unit between the amide linkages. The selection of this reagent was based on its potential to influence biological activity through spatial orientation and conformational constraints. Although the structures of **7a** or **7b** have been previously reported [47], the original publication lacks essential experimental details such as the specific enantiomer of the chiral amine used and the synthetic methodology applied. In our study, these compounds were synthesized through a well-defined and reproducible synthetic route, with the enantiomeric identity of the starting materials clearly established. The ^{1}H and ^{13}C NMR spectra of compounds **7a** and **7b** were analyzed, revealing similar key peaks to those observed for compounds **5a–5d**. For compounds **7a** and **7b**, amide carbonyl bands are observed at 1674 and 1684 cm^{-1}, respectively, while the —CONH stretching vibrations appear around 3315 cm^{-1}. In addition, the LC–MS analysis results were consistent with the calculated molecular masses.

All target compounds (**5a–5d**, **7a**, and **7b**) were obtained in good yields and were thoroughly characterized by ^{1}H and ^{13}C NMR spectroscopy, LC–MS, and IR spectroscopy. The combined spectral data confirm the successful synthesis and structural integrity of the desired chiral amides (Figures S1–S40).

2.2 | Biological Activity Studies

The IC_{50} values, which represent the inhibitor concentration required to reduce enzyme activity by 50%, were used to evaluate the inhibitory effects of novel chiral anthranilic amide derivatives on AChE and BChE activity. For AChE, IC_{50} values of molecules **5a–5d**, **7a**, and **7b** were found to be 70, 63.64, 53.85, 36.84, 17.07, and 17.5 nM, respectively (Table 1). In vitro studies showed that **7a** and **7b** exhibited the best inhibitory effect on AChE among the tested compounds. These results showed that **7a** and **7b** had a more effective inhibitory ability compared to tacrine. This good result was credited to the influence of the spacer group. On the other hand, there was no selectivity between enantiomers pairs (**7a** and **7b**). The in vitro studies showed that the spacer group increased the inhibition effect but decreased enantioselectivity. While the inhibition profiles of molecules **5a**, **5b**, and **5c** were close to tacrine, molecule **5d** had a stronger inhibition effect than tacrine. When the **5a** and **5c** enantiomer were considered, it was seen that the *S*-enantiomer **5c** showed a better inhibition ability than **5a**. Similarly, when the **5b** and **5d** enantiomer pairs are compared, it was seen that the *S*-enantiomer exhibited superior inhibition activity compared to the *R*-enantiomer. Substitution of chloride on 2-position on the nicotinoyl chloride enhanced the inhibition effect for both enantiomers.

TABLE 1 | Inhibition results of novel chiral anthranilic acid derivatives (**5a–5d**, **7a**, and **7b**) derivatives on AChE and BChE activity.

Compounds	IC_{50}	
	AChE	BChE
7a (*R*)	17.07 nM	175 nM
7b (*S*)	17.5 nM	116.6 nM
5a (*R*)	70 nM	46.66 μM
5b (*R*)	63.64 nM	33.33 μM
5c (*S*)	53.85 nM	116.6 μM
5d (*S*)	36.84 nM	233.3 μM
Tacrine[a]	53.84 nM	11.29 nM

[a]Tacrine served as the reference inhibitor for both AChE and BChE in this study.

For BChE, IC_{50} values of **5a–5d**, **7a**, and **7b** was found to be 46.66 μM, 33.33 μM, 116.6 μM, 233.3 μM, 116.6 nM, and 175 nM, respectively (Table 1). When the inhibitory effects of compounds **5a–5d**, **7a**, and **7b** on BChE activity were evaluated in relation to tacrine, it became apparent that these molecules exhibited less potent inhibition compared to tacrine. All six compounds (**5a–5d**, **7a**, and **7b**) showed weaker inhibition effects for BChE than AChE. However, compounds **7a** and **7b** with spacer group structure showed the best inhibition effect on BChE activity as well as AChE (Figure 1). When the **5a** and **5c** enantiomers were considered, it was seen that the *R*-enantiomer **5a** showed a better inhibition effect than **5c** contrary to AChE. Similarly, when the **5b** and **5d** enantiomer pairs are compared, it was seen that the *R*-enantiomer showed a better inhibition effect than the *S*-enantiomer. An interesting result contrary to AChE was obtained when substituting chloride in 2-position on the nicotinoyl chloride. While this substitution enhanced the inhibition effect for the *R* configuration, diminished for the *S* configuration.

There are several studies in the literature evaluating anthranilic acid derivatives as ChE inhibitors, and the anthranilic acid-based

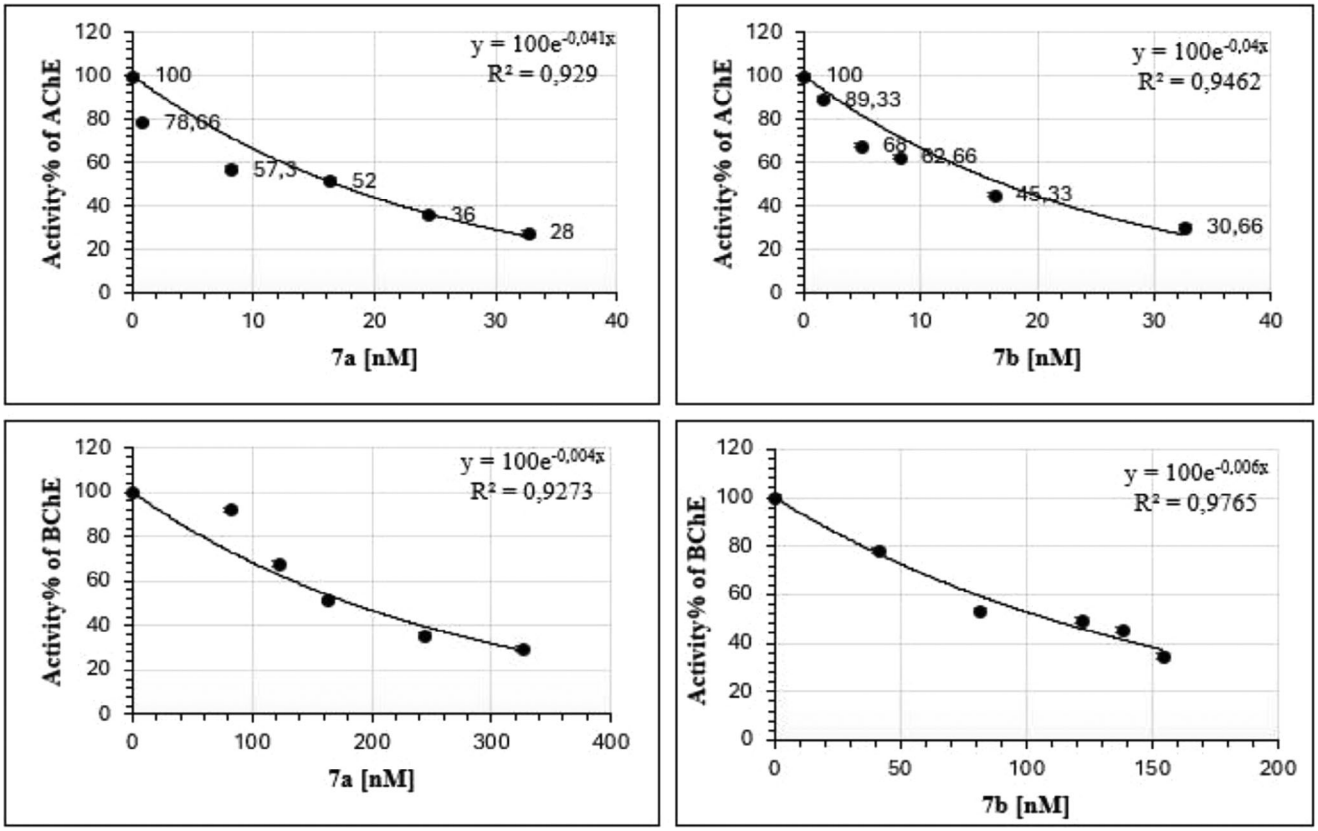

FIGURE 1 | IC_{50}/[inhibitor concentration] graphs of molecules **7a** and **7b** for AChE and BChE.

compounds examined in these studies were found to be strong inhibitors of ChEs. These studies support the results of the current study [48–50]. In addition, it is advantageous that the anthranilic acid derivatives evaluated as ChE inhibitors in this study have a chiral structure and may form the basis for research focused on discovering novel chiral inhibitors of AChE and BChE with pure enantiomer structures. The use of pure enantiomers in drug design studies is important in terms of preventing adverse drug reactions and making drugs more effective therapeutic agents [38, 39]. Therefore, determining the individual inhibition effects of the R and S enantiomers of molecules **5a–5d**, **7a**, and **7b** on AChE and BChE in this study makes the obtained results valuable.

2.3 | In Silico Docking Study

The structural model generated using the Prime module was visualized in the workspace as a ribbon representation, providing a detailed view of its overall conformation. To enhance interpretability, the model was automatically color-coded based on sequence conservation and similarity. Residues matching the template structure were highlighted in bold blue, while those with similar properties were marked in cyan for easy identification. In addition, sequence insertions were distinctly annotated, as illustrated in Supplementary Figure S41. Once the model was created, the focus shifted to rigorously examining its structural robustness, tackling any flaws like steric clashes, incorrect bond lengths, angle distortions, and other conformational inconsistencies. To refine the model and ensure structural accuracy, the Protein Preparation Wizard was employed, facilitating the correction of common structural discrepancies. A comparative sequence analysis revealed that the equine serum BChE enzyme shared a high degree of homology with the 7AIY crystal structure template. Specifically, the sequence identity was determined to be 90%, while the percentage of positive matches indicating highly conserved and functionally similar residues was calculated at 94%. These findings reinforce the reliability of the homology model, underscoring its suitability for further computational analyses and molecular docking studies. To further evaluate the structural reliability of the protein model generated through homology modeling, additional validation was conducted using the Verify3D and ERRAT online tools. The Verify3D assessment indicated that 93.17% of the amino acid residues achieved an average 3D-1D profile score of 0.1 or higher, suggesting strong compatibility between the modeled three-dimensional (3D) structure and its corresponding amino acid sequence. Meanwhile, the ERRAT analysis yielded an overall quality factor of 83.78, reflecting a high degree of structural precision. These validation metrics, presented in Figures S42 and S43, collectively support the credibility and accuracy of the constructed protein model. In addition, the alignment information has also been included in the Supporting Information (Figure S44).

The structural model, constructed with the Prime module of Schrödinger Maestro, was put through a rigorous assessment via the Ramachandran plot, leaving no stone unturned in ensuring its flawless integrity. This plot offers a graphical representation of the distribution of residues based on their phi (φ) and psi (ψ) dihedral angles, providing valuable insights into the

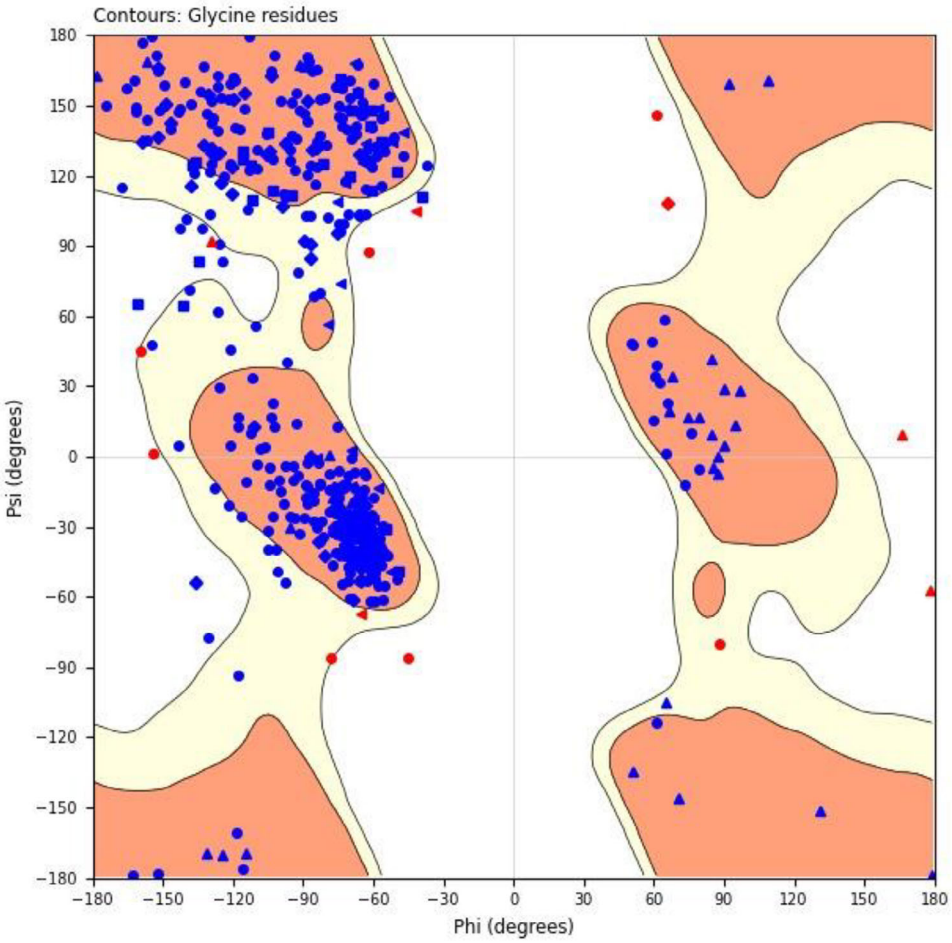

FIGURE 2 | Ramachandran plot revealing the structural integrity of the modeled protein.

conformational quality of the model. Residues located within the permissible zones are marked in yellow, the ones in the preferred zones are shaded reddish-orange, whereas residues that fall outside the acceptable boundaries are displayed in white. Figure 2 clearly shows that most residues are securely placed within the allowed regions, with only a small number deviating into the disallowed zones. This strongly indicates that the model maintains stellar stereochemical integrity and aligns precisely with expected structural constraints.

Induced-fit docking (IFD) methodology was employed to delve into the binding interactions of novel chiral anthranilic acid derivatives (**5a–5d**, **7a**, and **7b**) with AChE and BChE enzymes. This approach provided a deeper understanding of the inhibitory effects exhibited by these compounds. Tacrine, a widely recognized inhibitor for both enzymes, was included as the positive control for comparison. In addition, the Prime molecular mechanics/generalized born surface area (MM/GBSA) module was employed to compute the free binding energies, providing a deeper understanding of the thermodynamic factors influencing the interaction between the compounds and the enzymes. The docking scores and MM/GBSA values are presented in Table 2, which highlights the strength and stability of these interactions.

The results of the molecular docking studies aligned well with the in vitro inhibition data. Compounds **7a** and **7b**, known for their potent inhibition of AChE, achieved the highest docking scores and free binding energies, reinforcing the experimental findings. These compounds demonstrated superior anti-AChE activity compared to tacrine, further confirmed by the in silico data. In addition, the docking and MM/GBSA simulations for BChE confirmed the in vitro inhibition profiles of **5a–5d**, **7a**, and **7b**, though the same level of accuracy was not reached for tacrine's interaction with BChE, highlighting a discrepancy between the computational model and experimental data for the positive control (Table 2).

Among the studied compounds, **7b** stood out for its remarkable inhibitory effect on AChE, earning the highest docking score of −15.301 kcal/mol. The MM/GBSA simulations for **7b** revealed a significantly low free binding energy of −116.36 kcal/mol (Table 2), confirming its high affinity for the AChE enzyme. Within the enzyme's active site, **7b** formed π–π interactions with key residues such as TYR70, TRP84, and PHE330, while also establishing dual hydrogen bonds with TYR121. Additional hydrogen bonds were formed through water molecules interacting with ASP72, GLN74, and SER81, which further solidified the complex (Figure 3A).

When tested against BChE, **7b** again emerged as a top performer, achieving the highest docking score of −13.238 kcal/mol and a free binding energy of −83.19 kcal/mol (Table 2). The in silico analysis

TABLE 2 | Induced-fit docking scores (kcal/mol) and MM/GBSA binding energy (kcal/mol) results for the chiral anthranilic acid derivatives (**5a–5d**, **7a**, and **7b**), showing potent inhibition activity.

	AChE		BChE	
Compound	**IFD docking score**	**MM/GBSA (ΔG_{bind})**	**IFD docking score**	**MM/GBSA (ΔG_{bind})**
5a (*R*)	−9.564	−69.92	−7.971	−46.28
5b (*R*)	−9.317	−58.86	−8.208	−49.46
5c (*S*)	−10.364	−55.94	−7.960	−53.61
5d (*S*)	−11.353	−77.25	−8.909	−46.30
7a (*R*)	−14.474	−93.80	−12.481	−76.80
7b (*S*)	−15.301	−116.36	−13.238	−83.19
Tacrine[a]	−11.338	−75.88	−6.566	−53.24

[a]Tacrine used as reference inhibitor for AChE and BChE.

showed that **7b** formed hydrogen bonds with critical residues in the BChE active site, namely, LEU285 and TYR332, corroborating its strong anti-BChE activity (Figure 3B).

2.4 | ADME Analysis

A thorough assessment of the drug-likeness and pharmacokinetic properties of the novel chiral anthranilic acid derivatives (**5a–5d**, **7a**, and **7b**) was conducted using the QikProp module in the Maestro software suite. This evaluation provided crucial insights into the compounds' physicochemical characteristics, membrane permeability, metabolic stability, and overall pharmaceutical potential. Since successful drug candidates must demonstrate optimal ADME properties, a detailed computational analysis was necessary to determine their suitability for therapeutic applications.

MW plays a pivotal role in defining a drug's absorption and distribution. All analyzed compounds had MW values within the optimal range, aligning with Lipinski's rule of five, which suggests that molecules below 500 Da are more likely to exhibit favorable pharmacokinetic properties.

Permeability across biological membranes is another key determinant of oral bioavailability. The apparent permeability coefficient (QPPCaco) of the derivatives, which predicts their ability to cross the intestinal epithelium via passive diffusion, ranged from 528.095 to 2,033.448 nm/s. These values suggest efficient gastrointestinal absorption, an essential requirement for orally administered drugs.

Another crucial factor influencing absorption and tissue distribution is lipophilicity, represented by the octanol/water partition coefficient (QPlogPo/w). With values ranging from 3.719 to 7.556, these compounds display sufficient lipophilicity to facilitate membrane penetration while maintaining an acceptable balance with aqueous solubility. Excessive lipophilicity, however, can compromise metabolic stability and lead to poor water solubility. To address this, water solubility (QPlogS) was also examined, yielding values between −4.225 and −9.983. Although these values suggest moderate to low solubility in aqueous environments, they remain within acceptable pharmaceutical limits.

Cell permeability predictions using the Madin-Darby canine kidney (MDCK) model further supported the favorable absorption potential of these derivatives. The calculated QPPMDCK values ranged from 248.105 to 2185.709, reinforcing their ability to effectively traverse cellular barriers.

Ensuring drug safety is just as critical as optimizing its efficacy. One of the major concerns in drug development is the potential for cardiotoxicity, particularly through the inhibition of the human ether-a-go-go-related gene (hERG) potassium channel, which can lead to fatal cardiac arrhythmias. The QPlogHERG values for all tested compounds were found to be below −5, indicating a low risk of hERG-related toxicity.

High human oral absorption (%HOA) values, ranging from 90.891% to 100%, further reinforce the potential of these derivatives as effective oral drug candidates. Their ability to be efficiently absorbed into the bloodstream makes them promising for systemic therapeutic applications.

Despite their potent inhibitory activity against AChE and BChE targets relevant to neurological disorders like AD the derivatives **5a−5d**, **7a**, and **7b** exhibit limited blood–brain barrier (BBB) permeability, as indicated by negative QPlogBB values (−1.647 to −0.258). This constraint likely arises from their high MWs (≈612 for **7a**/**7b**) and elevated lipophilicity (QPlogPo/w > 7), which exceed optimal ranges for passive BBB penetration and violate drug-likeness guidelines. Structural optimization to reduce MW or modulate lipophilicity could enhance BBB accessibility while retaining enzymatic inhibition, thereby improving their potential as CNS-targeted therapeutics.

Altogether, the pharmacokinetic analysis suggests that these anthranilic acid derivatives meet critical ADME criteria and exhibit a well-balanced profile of solubility, permeability, metabolic stability, and safety (Table 3). Their physicochemical and pharmacological properties align with those of clinically approved drugs, positioning them as promising candidates for further preclinical and clinical investigations. These findings

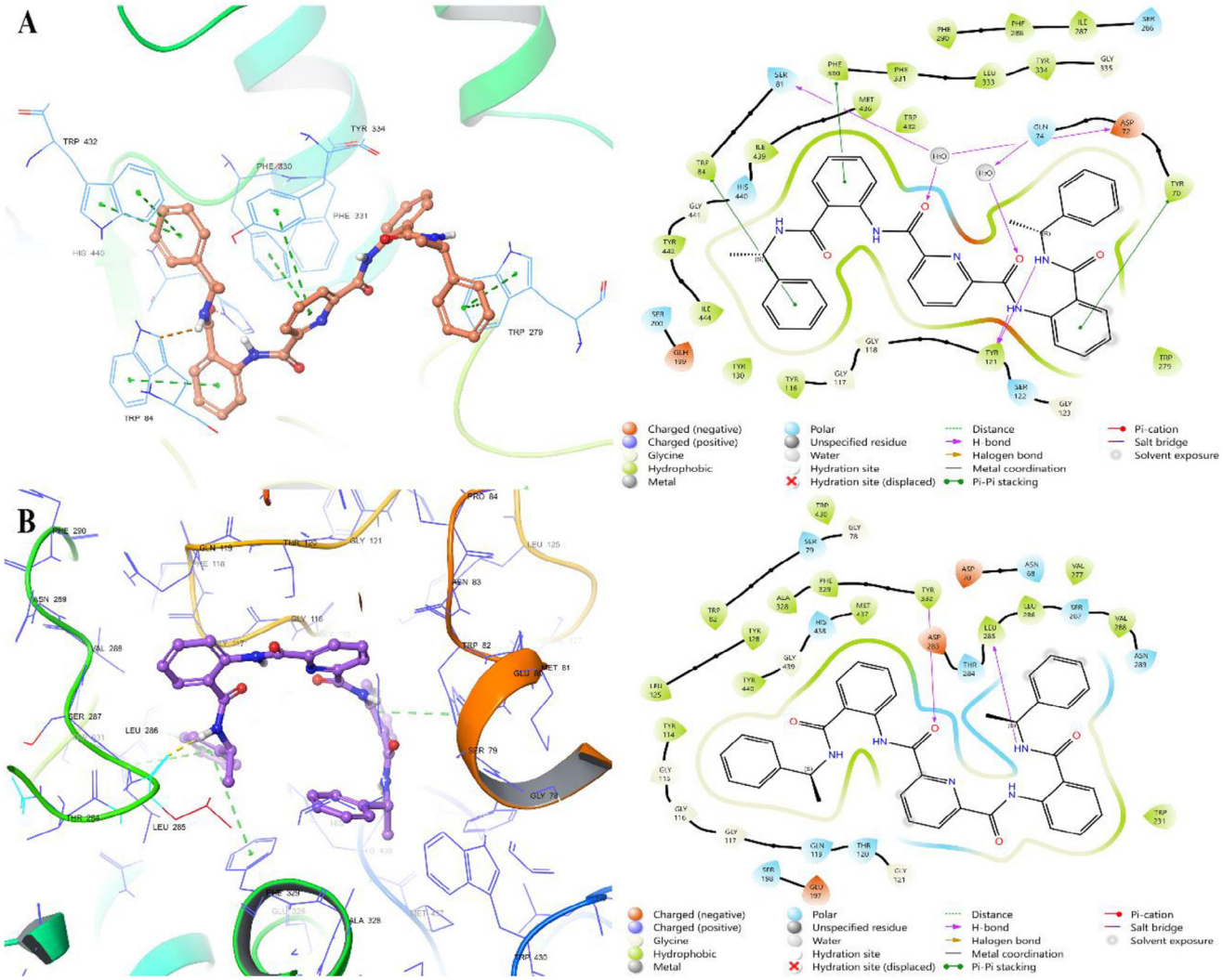

FIGURE 3 | The left panel offers a detailed 3D view of the docking pose, while the right panel provides a clear 2D map of how compound **7b** interacts with AChE (A) and BChE (B).

highlight their potential role in drug discovery, particularly in the medication of neurodegenerative diseases.

2.5 | MD Simulation

While docking studies offer a static view of how a molecule binds to a protein's active site, MD simulations provide a dynamic analysis, capturing atomic movements over time according to Newton's laws of motion [51]. To delve deeper into the stability and key interactions of the ligand–protein complex, MD simulations were performed for compound **7b**. This compound was selected due to its outstanding in vitro inhibition, impressive docking score, and strong MM/GBSA binding free energy. The resulting simulation data for the **7b**–AChE and **7b**–BChE complexes are shown in Figures 3 and 4, respectively.

A detailed breakdown of hydrogen bonding interactions in the AChE enzyme's active site is presented in Figure 4A, where purple arrows indicate key interactions. Throughout the simulation, compound **7b** established persistent hydrogen bonds with crucial residues, including TRP84 (54% of the simulation time), TRP279 (36%), PHE290 (32%), GLU199 (71%), and PHE330 (68% and 42%). The strong and sustained interactions, particularly with TRP84, GLU199, and PHE330, likely perform a vital role in the enhanced stability of the ligand–protein complex.

Figure 4B illustrates the root mean square deviation (RMSD) plots, providing insights into system stability. The average RMSD value for the protein's Cα atoms (left *Y*-axis) was approximately 1.8 Å (pale blue), while the ligand's RMSD (right *Y*-axis) stabilized at around 3 Å (red) when fitted to the protein. Although minor deviations from the initial position were observed, both the ligand and protein maintained stable RMSD values throughout the simulation, falling within the acceptable thermal fluctuation range of 1–3 Å, indicative of a well-maintained complex.

The flexibility of amino acid residues in AChE influenced by **7b** binding is visualized in Figure 4C through root mean square fluctuation (RMSF) analysis. Green vertical bars highlight the residues that directly interact with the ligand. The consistently low RMSF values of these interacting residues suggest strong, favorable contacts, contributing to the overall structural stabilization of the enzyme–ligand system.

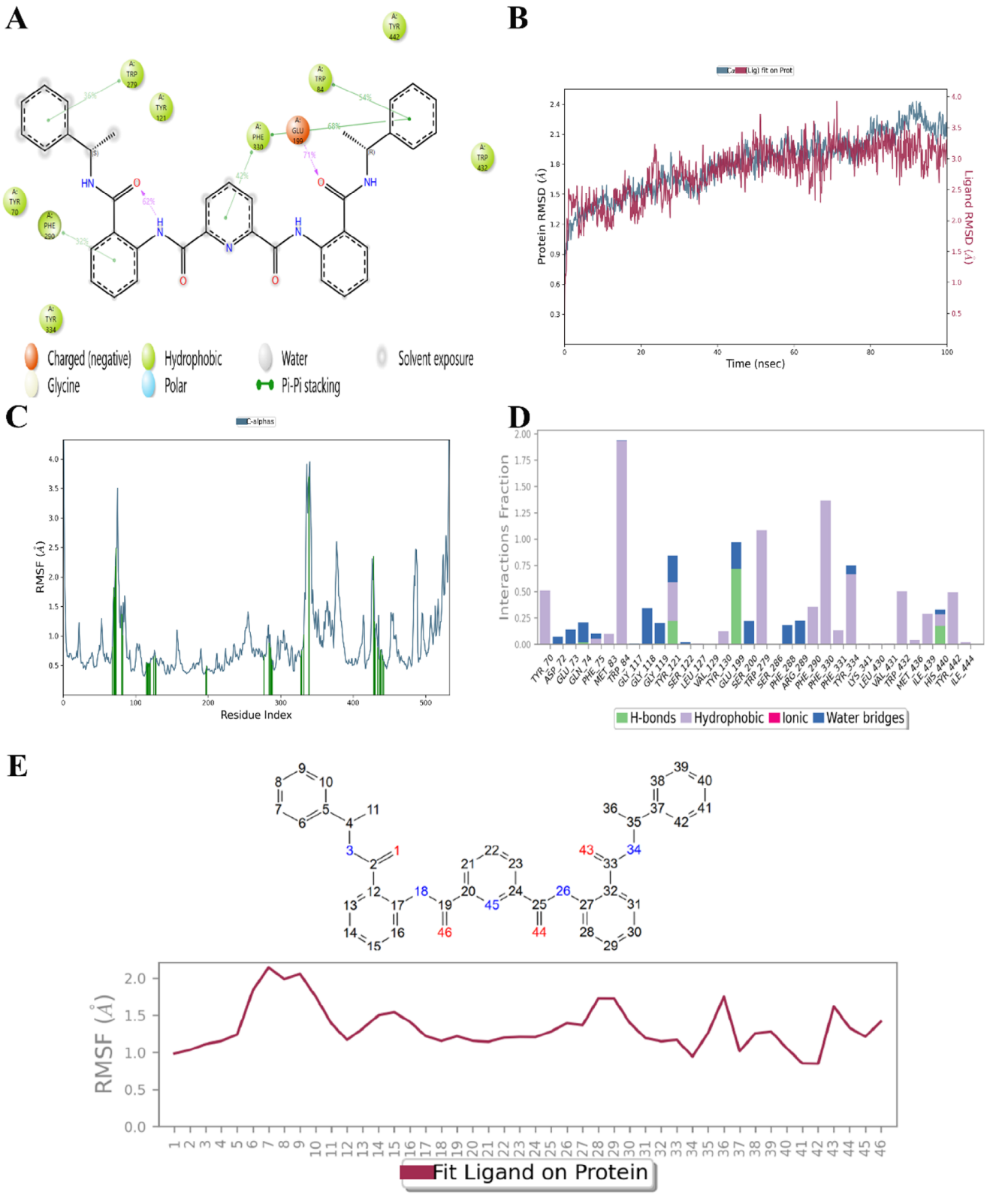

FIGURE 4 | Figures illustrating protein–ligand contacts (A), RMSD of the protein and ligand (B), RMSF (C), protein–ligand interactions histogram (D), and ligand RMSF (E) for the AChE–**7b** complex.

TABLE 3 | Analysis of the predicted ADME (absorption, distribution, metabolism, and excretion) properties for compounds **5a–5d**, **7a**, and **7b**.

Compound	mol MW	QPlogS	QPlogPo/w	QPlogHERG	QPlogBB	QPPCaco	%HOA	QPPMDCK	RuleOfFive	RuleOfThree
5a (*R*)	345.400	−5.074	4.557	−5.530	−0.258	1896.060	100.000	2185.709	0	0
5b (*R*)	379.845	−5.117	4.549	−5.587	−0.276	1836.906	100.000	2111.999	0	0
5c (*S*)	345.400	−4.225	3.719	−5.535	−0.541	1339.434	100.000	678.480	0	0
5d (*S*)	379.845	−4.544	3.950	−6.059	−0.406	2.033.448	100.000	1065.402	0	0
7a (*R*)	611.699	−9.079	7.025	−8.878	−1.647	528.095	90.891	248.105	2	1
7b (*S*)	611.699	−9.983	7.556	−9.779	−1.408	974.323	100.000	480.993	2	1
Tacrine[a]	198,267	−3.141	2.594	−4.168	0.037	2931.418	100.000	1581.998	0	0

[a]Tacrine used as reference inhibitor for AChE and BChE.

Figure 4D presents a detailed histogram of ligand–protein interactions throughout the 100-ns simulation, categorizing them based on interaction type. Green bars indicate hydrogen bonding interactions, purple represents hydrophobic contacts, and blue denotes water-mediated hydrogen bonds. This distribution of interaction types further reinforces the dynamic stability of compound **7b** within the enzyme's active site, supporting its potential as a encouraging contender for enzyme inhibition.

Figure 4E shows the per-atom RMSF profile of the **7b** ligand bound to the AChE protein, highlighting its flexibility during the MD simulation. After fitting the trajectory to the protein, fluctuations reflect only internal ligand motion. The highest flexibility is observed in the aromatic ring region (atoms 6–10), suggesting solvent exposure or weak interactions. In contrast, the central linker (atoms 18–26) remains relatively stable, likely due to strong binding interactions. Overall, the ligand exhibits a mostly rigid conformation with localized flexibility, which may inform future optimization strategies.

Figure 5A demonstrates the hydrogen bond interactions (shown by purple arrows) between compound **7b** and the residues TRP82 (34% of the simulation time), TYR332 (37% of the simulation time), ALA328 (38% of the simulation time), ASN68 (46% of the simulation time), ASP70 (59% of the simulation time), SER79 (65% of the simulation time), and GLY116 (35% of the simulation time) within the active site of the BChE enzyme. The consistent hydrogen bonding of residues SER79 and ASP70 with the BChE protein for most of the simulation time likely plays a key role in the complex's enhanced stability. Figure 5B presents the RMSD plots for both the ligand and the protein, illustrating the system's stability. The average RMSD value for the protein's Cα atoms (left *Y*-axis) was approximately 1.9 Å (pale blue), whereas the ligand's average RMSD value (right *Y*-axis), when fitted to the protein, was around 3 Å (red). The protein's RMSD value slightly deviated from its initial position around 30 ns but stabilized for the rest of the simulation. Similarly, the ligand's RMSD value also deviated slightly from its initial position but maintained a steady value of around 3 Å throughout the simulation. In both instances, the RMSD values for the protein showed minor deviations from their initial positions but stayed within the acceptable thermal range of 1–3 Å, indicating stable binding. Figure 5C shows the RMSF of the protein, which measures the flexibility of amino acid residues in the BChE enzyme influenced by **7b**. The residues that interact with the ligand are highlighted with green vertical lines. These interacting residues exhibit low RMSF values, suggesting that the ligand forms favorable contacts, contributing to the overall stabilization of the system. Figure 5D displays histograms of the interaction fractions, detailing the ligand's interactions with key protein residues over the 100-ns simulation period. The green columns indicate hydrogen bond interactions, the purple columns represent hydrophobic interactions, and the blue columns signify water-mediated hydrogen bond interactions. Figure 5E presents the per-atom RMSF profile of the **7b** ligand during MD simulation, aligned to the BChE protein to isolate internal ligand flexibility. The highest RMSF values (~1.6 Å) are observed around atoms 6–9, indicating notable mobility in this region, likely due to limited stabilizing interactions with the protein. In contrast, the central core of the ligand (atoms 18–26) shows lower fluctuations (< 1.0 Å), reflecting a more rigid and stable conformation within the binding pocket. Moderate

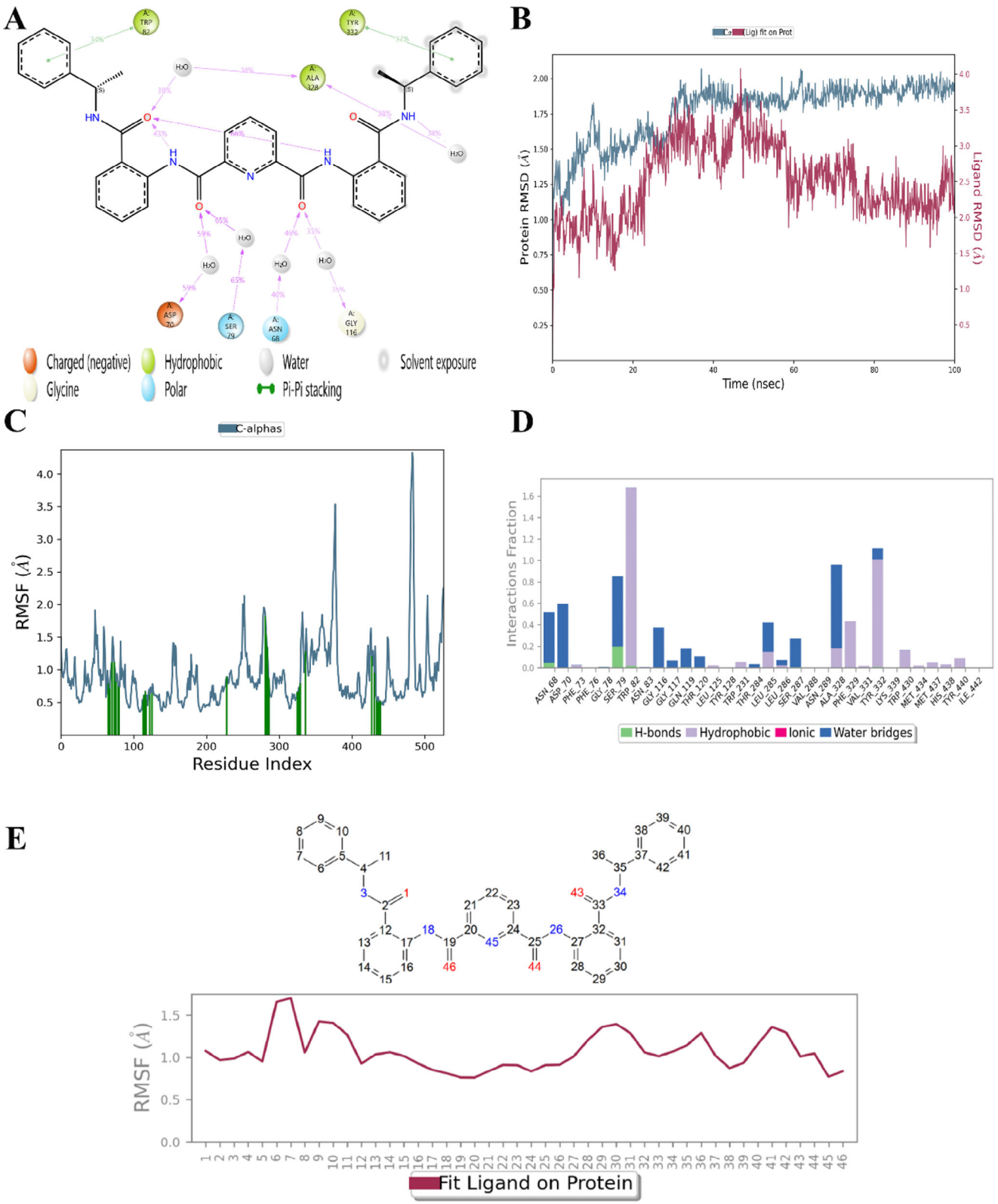

FIGURE 5 | Figures illustrating protein–ligand contacts (A), RMSD of the protein and ligand (B), RMSF (C), protein–ligand interactions histogram (D), and ligand RMSF (E) for the BChE–**7b** complex.

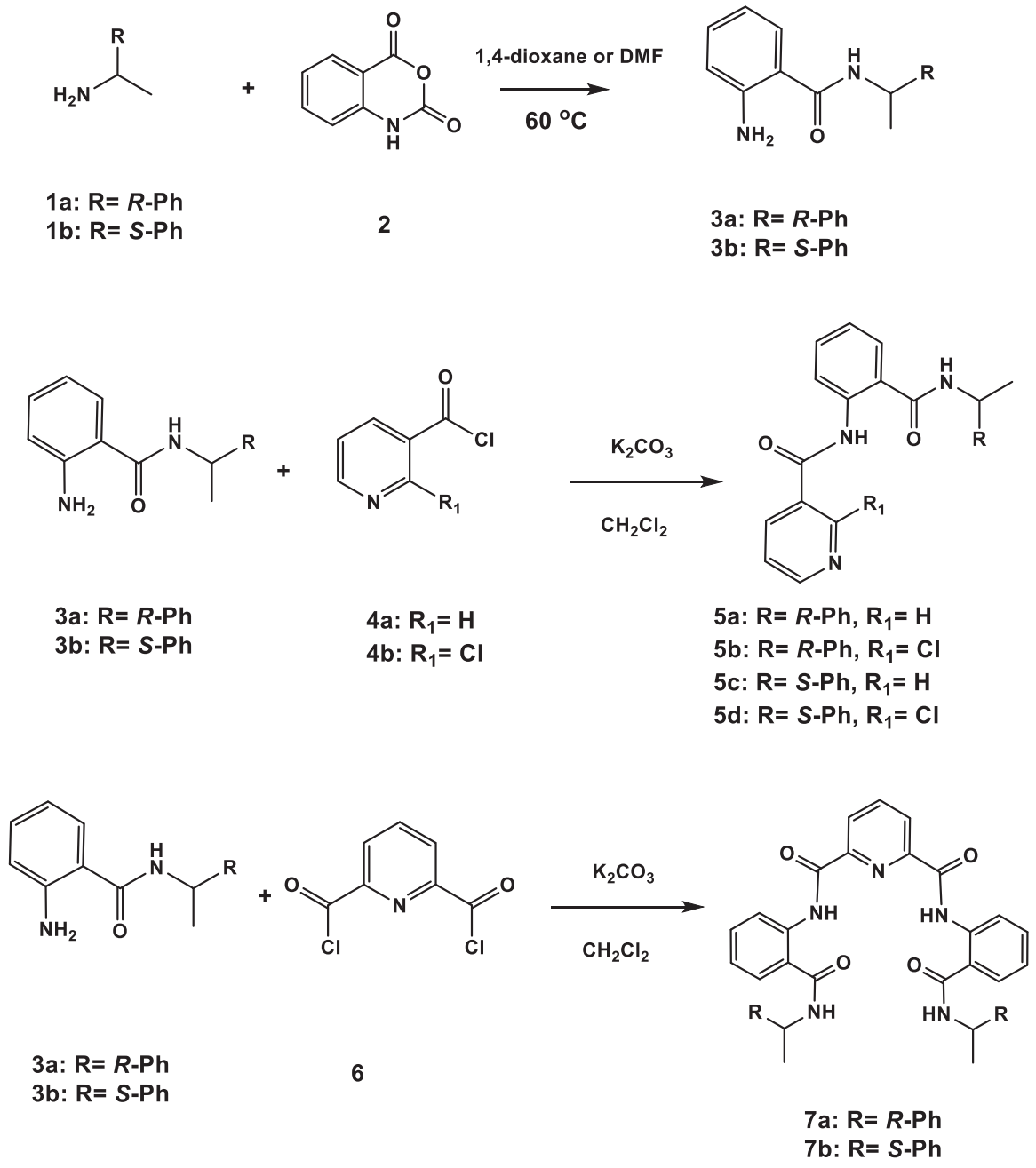

SCHEME 1 | Synthesis of chiral anthranilic amide derivatives.

flexibility is also noted in the terminal aromatic ring (atoms 35–41), suggesting partial solvent exposure. These results highlight structurally stable and flexible regions of the ligand, offering insight into interaction dynamics and potential sites for further optimization.

3 | Conclusion

One of the goals of drug discovery studies is to find therapeutic agents that can bind to the active site of an enzyme that is important in the relevant disease and change the activity of the enzyme, thus improving the symptoms of the disease. In the development of treatments for AD, the primary therapeutic focus revolves around inhibitors of AChE and BChE enzymes. In this study, new chiral anthranilic amide derivatives (**5a–5d**, **7a**, and **7b**) were synthesized and their inhibition effects on both AChE and BChE activity were examined. All molecules (**5a–5d**, **7a**, and **7b**) showed stronger inhibition effects on AChE activity than BChE. The chiral structure of the molecules caused different biological activities on both enzymes. In this respect, the results of the study are valuable. Enantioselective inhibition was observed in compounds **5a–5d**. *S* enantiomers had a better inhibition effect than *R*-enantiomers for AChE, while *R*-enantiomers showed a stronger inhibition effect for BChE. **7a** and **7b** exhibited a much stronger inhibition effect than **5a–5d** on both AChE and BChE activity due to the effect of the spacer group in the structure. However, despite the potency inhibition effect, the enantioselectivity decreased in **7a** and **7b**. Molecular docking analyses of compounds **5a–5d**, **7a**, and **7b** revealed strong interactions

with both AChE and BChE enzymes, exhibiting high binding affinities. Among them, compound **7b** demonstrated the most favorable binding energy with AChE, reaching −15.301 kcal/mol, suggesting a particularly strong interaction. Furthermore, ADME assessments highlighted that all tested chiral anthranilic amide derivatives (**5a–5d**, **7a**, and **7b**) possess excellent gastrointestinal absorption while displaying limited permeability through the skin. These pharmacokinetic properties indicate a promising drug-like profile for targeting AChE and BChE proteins. In summary, the findings from this study provide valuable insights into the potential of these molecules as enzyme inhibitors, laying the groundwork for the rational design and synthesis of novel chiral AChE and BChE inhibitors. These findings may provide a basis for the creation of therapeutic drugs designed to treat AD and other related neurological disorders.

4 | Experimental Section

4.1 | Materials

Enzymes (BChE: CAS no. 9001-08-5; AChE: CAS no. 9000-81-1) and chemicals utilized in inhibition studies were supplied by Sigma-Aldrich Co. (Sigma-Aldrich Chemie GmbH, Germany). Chiral amines, solvents, and reagents used in synthesis studies were purchased from Sigma-Aldrich. The DMF was dried prior to use. IR spectra were obtained using a Nicolet-6700 ATR-FT-IR spectrophotometer, covering the 4000–400 cm^{-1} range. Melting points were determined with a Thermo Fisher Scientific Electrothermal 9100 apparatus. ^1H NMR (300 MHz) and ^{13}C NMR (100 MHz) spectra were recorded at room temperature on a Bruker Ultrashield spectrometer, with TMS as the reference. Mass spectra were acquired using a Thermo Scientific TSQ Quantum Access Max LC–MS spectrometer in a methanol/acetonitrile mixture. Optical rotations were measured with an Anton Paar MCP100 polarimeter. In vitro inhibition studies were conducted using a Thermo GENESYS 10S UV–Vis spectrophotometer.

4.2 | General Procedure for the Synthesis of Compound (3a, 3b)

The isatoic anhydride was treated with [(*R*)-(+)-phenylethylamine, (*S*)-(−)-phenylethylamine, according to literature procedure [41–43].

4.2.1 | (*R* and *S*)-2-Amino-*N*-(1-Phenylethyl) Benzamide (3a and 3b)

Isatoic anhydride **2** (2.45 g, 15 mmol) and the (*R*)-(+)-phenylethylamine **1a** or (*S*)-(−)-phenylethylamine **1b** (2.18 g, 18 mmol) in anhydrous 1,4-dioxane or DMF (13 mL) were stirred under an atmosphere of nitrogen at 60°C for 6 h. Filtration of the mixture through charcoal and concentration on a rotary evaporator yield 3.50 g (97%) of the desired benzamide **3a** and **3b**, as a white solid: mp 135°C–137°C, ^1H NMR (400 MHz, $CDCl_3$): δ 1.559–1.77 (d, J = 7.2 Hz, 3H), 5.229-5.299 (p, J = 7.0 Hz, 1H), 5.516 (bs, 2H, NH_2), 6.365–6.383 (d, J = 7.2 Hz, 1H), 6.608–6.667 (q, J = 7.9 Hz, 2H), 7.126–7.228 (m, 2H), 7.257–7.290 (t, J = 6.6 Hz, 1H), 7.328–7.388 (m, 5H); ^{13}C NMR (100 MHz, $CDCl_3$): δ 22.23, 48.92, 116.22, 116.78, 117.56, 126.36, 127.39, 127.58, 128.96, 132.55,143.61, 149.02, 168.73. LC–MS (m/z): Calcd. for $C_{15}H_{16}N_2O$ [M + H] 240.13, found: 240.84.

4.3 | General Procedure for the Synthesis of Compound (5a–5d)

A mixture of **3a** or **3b** (0.5 g, 2.08 mmol), and K_2CO_3 (1.41 g, 10 mmol) were dissolved in DCM (20 mL), nicotinoyl chloride hydrochloride **4a** (0.55 g, 3.12 mmol), the 2-chloronicotinoyl chloride **4b** (0.5 g, 3.12 mmol) was added slowly to the mixture and stirred for 6 h at room temperature. The resulting mixture was allowed to react at room temperature, with substrate conversion monitored by TLC analysis. Subsequently, the solvent was removed under reduced pressure, and the crude product was purified by recrystallization with a blend of ethyl acetate and hexane to yield desired compounds **5a–5d** according to the modified literature procedure [52].

4.3.1 | (*R*)-*N*-(2-((1-Phenylethyl)Carbamoyl)Phenyl) Nicotinamide (5a)

White solid, yield (0.590 g 82%), mp 178°C–180°C, ^1H NMR (400 MHz, $CDCl_3$): δ 1.618–1.635 (d, J = 6.8 Hz, 3H), 5.279–5.350 (p, J = 7.1 Hz, 1H), 6.941–6.960 (d, J = 7.6 Hz, 1H), 7.009–7.045 (t, J = 7.2 Hz, 1H), 7.258–7.291 (t, J = 6.6 Hz, 1H), 7.333–7.446 (m, 6H), 7.523–7.546 (dd, J_1 = 7.6, J_2 = 1.4 Hz, 1H), 8.203–8.23(dt, J_1 = 8, J_2 = 2 Hz, 1H), 8.678–8.699 (d, J = 8.4, 1H), 8.714–8.730(dd, J_1 = 4.8 Hz, J_2 = 1.6 Hz, 1H) 9.226–9.231(d, J = 2 Hz, 1H), 12.280 (s, 1H); ^{13}C NMR (100 MHz, $CDCl_3$): δ 21.89, 49.66, 120.59, 121.73, 123.40, 123.70, 126.44, 126.98, 127.90, 129.06, 130.63, 132.97, 135.08, 139.76, 142.77, 149.32 (t, J = 43.5 Hz), 152.63, 163.94, 168.57. LC–MS (m/z): Calcd. for $C_{21}H_{19}N_3O_2$ [M + H] 345.40, found: 345.79.

4.3.2 | (*R*)-2-Chloro-*N*-(2-((1-Phenylethyl)Carbamoyl) Phenyl)Nicotinamide (5b)

White solid, yield (0.662 g 84%), mp 143°C–145°C, ^1H NMR (400 MHz, $CDCl_3$): δ 1.576–1.594 (d, J = 7.2 Hz, 3H), 5.196–5.267 (p, J = 7.1 Hz, 1H), 6.659–6.678 (d, J = 7.5 Hz, 1H), 7.103–7.141 (t, J = 7.6 Hz, 1H), 7.280–7.356 (m, 6H), 7.483–7.537 (q, J = 7.3 Hz, 2H), 7.893–7.917 (dd, J_1 = 7.5, J_2 = 1.8 Hz, 1H), 8.455–8.471(dd, J_1 = 4.7, J_2 = 1.7 Hz, 1H), 8.674–8.695 (d, J = 8.3 Hz, 1H), 11.629 (s, 1H); ^{13}C NMR (100 MHz, $CDCl_3$): δ 21.94, 49.67, 121.30, 122.06, 122.82, 123.98, 126.34, 126.85, 127.93, 129.09, 132.76, 132.97, 138.51, 139.05, 142.68, 148.10, 151.11, 164.00, 168.12. LC–MS (m/z): Calcd. for $C_{21}H_{18}ClN_3O_2$ [M + H] 379.11, found: 379.78.

4.3.3 | (*S*)-*N*-(2-((1-Phenylethyl)Carbamoyl)Phenyl) Nicotinamide (5c)

White solid, yield (0.560 g 78%), mp 178°C–180°C, ^1H NMR (400 MHz, $CDCl_3$): δ 1.620–1.638 (d, J = 7.2 Hz, 3H), 5.282–5.353 (p, J = 7.1 Hz, 1H), 6.852–6.871 (d, J = 7.6 Hz, 1H), 7.026–7.067 (td, J_1 = 8 Hz, J_2 = 1.1 Hz, 1H), 7.258–7.297 (t, J = 7.8 Hz, 1H), 7.338–7.468 (m, 6H), 7.521–7.544 (dd, J_1 = 7.6, J_2 = 1.6 Hz, 1H), 8.212–8.242 (dt, J_1 = 8, J_2 = 2.6 Hz, 1H), 8.696–8.740 (m, 2H),

9.233–9.239(d, J = 2.4 Hz, 1H), 12.285 (s, 1H); ^{13}C NMR (100 MHz, $CDCl_3$): δ 21.89, 49.67, 120.56, 121.76, 123.41, 123.70, 126.44, 126.92, 127.92, 129.07, 130.63, 133.01, 135.09, 139.80, 142.74, 149.32 (t, J = 43.5 Hz), 152.63, 163.95, 168.55. LC–MS (m/z): Calcd. for $C_{21}H_{19}N_3O_2$ [M + H] 345.40, found: 345.81.

4.3.4 | (*S*)-2-Chloro-*N*-(2-((1-Phenylethyl)Carbamoyl) Phenyl)Nicotinamide (5d)

White solid, yield (0.630 g, 80%), mp 143°C–145°C, ^{1}H NMR (400 MHz, $CDCl_3$): δ 1.563–1.580 (d, J = 6.8 Hz, 3H), 5.186–5.255 (p, J = 6.9 Hz, 1H), 6.801–6.819 (d, J = 7.2 Hz, 1H), 7.074–7.111 (t, J = 7.4 Hz, 1H), 7.258–7.345 (m, 6H), 7.452–7.491 (t, J = 7.8 Hz, 1H), 7.522–7.541 (d, J = 7.8 Hz, 1H), 7.867–7.889 (dd, J_1 = 7.6, J_2 = 1.2 Hz, 1H), 8.435–8.450 (dd, J_1 = 4.4, J_2 = 1.6 Hz, 1H), 8.648–8.668 (d, J = 8 Hz, 1H), 11.633 (s, 1H); ^{13}C NMR (100 MHz, $CDCl_3$): δ 21.94, 49.66, 121.32, 122.00, 122.84, 123.98, 126.34, 126.98, 127.89, 129.06, 132.73, 132.91, 138.48, 138.99, 142.75, 148.07, 151.11, 163.99, 168.14. LC–MS (m/z): Calcd. for $C_{21}H_{18}ClN_3O_2$ [M + H] 379.11, found: 379.78.

4.4 | General Procedure for the Synthesis of Compound (7a and 7b)

A mixture of **3a** or **3b** (0.5 g, 2.08 mmol), and K_2CO_3 (1.41 g, 10 mmol) were dissolved in DCM (20 mL), 2,6-pyridine carbonyl dichloride **6** (0.32 g, 1.56 mmol) was added slowly to the mixture and stirred for 6 h at room temperature. The resulting mixture was allowed to react at room temperature, with substrate conversion monitored by TLC analysis. Subsequently, the solvent was removed under reduced pressure, and the crude product was purified by recrystallization with a blend of ethyl acetate and hexane to yield desired compounds **7a** and **7b** according to the modified literature procedure [52].

4.4.1 | N^2,N^6-Bis(2-(((*R*)-1-Phenylethyl)Carbamoyl) Phenyl)Pyridine-2,6-Dicarboxamide (7a)

White solid, yield (0.940 g, 74%), mp 216°C–218°C, ^{1}H NMR (400 MHz, $CDCl_3$): δ 1.207–1.224 (d, J = 6.8 Hz, 6H), 4.872–4.944 (p, J = 7.2 Hz, 2H), 6.930–6.966 (d, J = 7.2 Hz, 6H), 7.00–7.055 (q, J = 6.2 Hz, 6H), 7.221–7.260 (t, J = 7.8 Hz, 2H), 7.502–7.540 (t, J = 7.6 Hz, 2H), 7.646–7.663 (d, J = 6.8 Hz, 2H), 8.059–8.098(t, J = 7.8 Hz, 1H), 8.230–8.250 (d, J = 8 2H), 8.323–8.343 (d, J = 8 Hz, 2H), 12.139 (s, NH); ^{13}C NMR (100 MHz, $CDCl_3$): δ 21.62, 49.42, 124.36, 125.11, 125.38, 126.12, 127.21, 127.42, 128.61, 128.74, 132.25, 136.64, 139.64, 142.77, 148.52, 162.57, 167.34. LC–MS (m/z): Calcd. for $C_{37}H_{33}N_5O_4$ [M + H] 611.25, found: 611.99.

4.4.2 | N^2,N^6-Bis(2-(((*S*)-1-Phenylethyl)Carbamoyl) Phenyl)Pyridine-2,6-Dicarboxamide (7b)

White solid, yield (0.966 g, 76%), mp 216°C–218°C, ^{1}H NMR (400 MHz, $CDCl_3$): δ 1.211–1.229 (d, J = 7.2 Hz, 6H), 4.875–4.947 (p, J = 7.2 Hz, 2H), 6.907–6.971 (m, 6H), 7.002–7.057 (m, 6H), 7.224–7.261 (t, J = 7.2 Hz, 2H), 7.503–7.545 (m, 2H), 7.644–7.667 (dd, J_1 = 8 Hz, J_2 = 1.6 Hz, 2H), 8.062–8.101 (t, J = 8 Hz, 1H), 8.233–8.253 (d, J = 8 2H), 8.326–8.346 (d, J = 8 Hz, 2H), 12.142 (s, NH); ^{13}C NMR (100 MHz, $CDCl_3$): δ 21.62, 49.43, 124.37, 125.11, 125.38, 126.12, 127.19, 127.43, 128.61, 128.73, 132.26, 136.65, 139.64, 142.76, 148.52, 162.58, 167.35. LC–MS (m/z): Calcd. for $C_{37}H_{33}N_5O_4$ [M + H] 611.25, found: 611.93.

4.5 | Inhibition Studies on ChEs (AChE and BChE)

AChE and BChE activities were evaluated based on the spectrophotometric method established by Ellman et al. [53, 54]. The procedure follows this principle: Acetylthiocholine iodide served as the substrate for AChE activity, while butyrylthiocholine iodide was used for BChE activity. AChE catalyzes the hydrolysis of acetylthiocholine iodide, producing acetic acid and thiocholine, whereas BChE hydrolyzes butyrylthiocholine iodide into butyric acid and thiocholine. The thiocholine generated from this reaction interacts with DTNB (Ellman's reagent, 5,5′-dithiobis(2-nitrobenzoic acid)), which is present in the reaction mixture, to produce a yellow compound 5-thio-2-nitrobenzoic acid. The intensity of the resulting yellow color was quantitatively measured through the rise in absorbance at 412 nm measured by a spectrophotometer, reflecting the enzymatic activity. The enzyme unit was calculated using the molar absorption coefficient of 5-thio-2-nitrobenzoic acid at 412 nm (13 600 M^{-1} cm^{-1}).

The inhibitory effects of **5a–5d**, **7a**, and **7b** on AChE and BChE activity were determined by measuring AChE and BChE activity for at least five concentrations including compounds **5a–5d**, **7a**, and **7b**. For the substances showing inhibitory effect, we calculated the %Activities of AChE and BChE against at least five different inhibitor doses. The inhibitor concentrations studied were determined by preliminary experiments. The enzyme activity of the control without inhibitor was accepted as 100%. The reference inhibitor, tacrine, was also subjected to the same experiment. All experiments were repeated three times. %Activity graphs were created against inhibitor concentrations for both the reference inhibitor and the compounds showing inhibitory effect (Figure 1; Figures S45 and S46). The IC_{50} values, which indicate the inhibitor concentration needed to reduce enzyme activity by 50%, were calculated using the equations of the curves obtained from these graphs.

4.6 | In Silico Studies

4.6.1 | Homology Modeling

Due to the lack of an experimentally determined 3D structure for equine serum BChE, a homology modeling strategy was implemented to construct its structural representation. The protein sequence of equine BChE, accessed under UniProt entry P81908, formed the basis for constructing a reliable model. To generate a robust comparative structure, the Prime Homology Modeling module was utilized, leveraging the crystal structure of human BChE (PDB ID: 7AIY) as a reference template. This tool seamlessly integrates fold recognition with homology modeling, enabling experienced users to fine-tune critical parameters to maximize predictive accuracy and structural fidelity [55, 56].

4.6.2 | Molecular Docking

Computational studies were carried out to investigate the binding interactions between a series of novel anthranilic amide derivatives (**5a–5d**, **7a**, and **7b**) and the enzymes AChE and BChE using IFD simulations [57]. These simulations, which build upon methodologies established in prior research [54, 58–61], were executed through Maestro 13.9 from the Schrödinger Molecular Modeling Suite [56], the structural model for AChE (PDB ID: 4TVK) was sourced from the RCSB Protein Data Bank. Meanwhile, the BChE enzyme structure was constructed through homology modeling, leveraging the crystallographic template with PDB ID: 7AIY as a guide. Prior to docking, both enzyme structures were refined and optimized at physiological pH conditions using the Protein Preparation Wizard [62]. To ensure an accurate representation of molecular interactions, the receptor structures underwent energy minimization utilizing OPLS4 force field. Starting with the native ligand-binding site in each enzyme, a receptor grid was generated. Meanwhile, the ligand molecules underwent thorough preparation and protonation at pH 7.0 ± 2.0 using the LigPrep module, ensuring that the simulation environment closely mirrors physiological conditions.

4.6.3 | Calculation of Binding Free Energy Using MM/GBSA

To further assess the stability and affinity of the ligand–enzyme complexes, binding free energies (ΔG_{bind}) were estimated using the MM/GBSA approach. This approach combines molecular mechanics calculations with implicit solvent models to deliver a precise estimation of the thermodynamic stability of protein–ligand interactions. The MM/GBSA computations were conducted using the Prime module, employing the OPLS4 force field alongside the VSGB solvation model to enhance the accuracy of the free energy estimates [63].

4.6.4 | ADME Studies

An in silico analysis of ADME was conducted to assess the pharmacokinetic profiles and drug-likeness of the anthranilic amide derivatives (**5a–5d**, **7a**, and **7b**). The QikProp module within Maestro 13.9 was utilized to predict key physicochemical and pharmacokinetic properties of these compounds. By comparing their characteristics to those of 95% of known pharmaceutical agents, QikProp facilitates a robust assessment of the compounds' potential for oral bioavailability, metabolic stability, and overall suitability as drug candidates.

4.6.5 | MD Simulations

To gain deeper insights into the dynamic stability of the most promising ligand–enzyme complex, MD simulations were conducted using the Desmond software package developed by D.E. Shaw Research. The compound exhibiting the highest docking score for both AChE and BChE was selected for further analysis. The protein–ligand complex was generated using the Desmond System Builder module and placed within an orthorhombic simulation box, with a 10 Å buffer zone around the protein. To create a realistic biological environment, explicit solvation was applied using the TIP3P water model, and NaCl counterions were introduced at a concentration of 0.15 M to neutralize the system.

Following system setup, energy minimization was performed using the OPLS4 force field to remove steric clashes and ensure system stability. The equilibrated complex was then subjected to a 100-ns MD simulation under isothermal–isobaric conditions (constant temperature of 300 K and pressure of 1 bar) with a time step of 2.5 fs. The RESPA integrator was employed to enhance computational efficiency. Throughout the simulation, key parameters such as ligand–protein interactions and conformational stability were analyzed. Structural deviations of the protein were assessed through the calculation of the RMSD of Cα atoms, while the ligand's stability within the binding pocket was evaluated based on the RMSD of its heavy atoms. These analyses provided valuable insights into the dynamic behavior and binding persistence of the ligand within the enzyme's active site.

Author Contributions

Chiral anthranilic amide derivatives were synthesized by Turgay Tunç and Nadir Demirel. Inhibition studies on AChE and BChE were conducted by Zuhal Alım. Molecular docking, molecular dynamics, and ADME analyses were performed by Namık Kılınç. The results were analyzed and the manuscript written by Zuhal Alım, Zuhal Kılınç, and Nadir Demirel.

Acknowledgments

The financial support of this work by the Kırşehir Ahi Evran University grant FEF.A3.24.006 and MMF.A3.24.002 is gratefully acknowledged.

Conflicts of Interest

The authors declare no conflicts of interest.

Data Availability Statement

The data that support the findings of this study are available in the Supporting Information of this article.

References

1. L. Guan, D. Peng, L. Zhang, J. Jia, and H. Jiang, "Design, Synthesis, and Cholinesterase Inhibition Assay of Liquiritigenin Derivatives as Anti-Alzheimer's Activity," *Bioorganic & Medicinal Chemistry Letters* 52 (2021): 128306.

2. G. L. Spada, D. V. Miniero, M. Rullo, et al., "Structure-Based Design of Multitargeting ChEs-MAO B Inhibitors Based on Phenyl Ring Bioisosteres: AChE/BChE Selectivity Switch and Drug-Like Characterization," *European Journal of Medicinal Chemistry* 274 (2024): 116511.

3. R. J. Obaid, N. Naeem, E. U. Mughal, et al., "Inhibitory Potential of Nitrogen, Oxygen and Sulfur Containing Heterocyclic Scaffolds Against Acetylcholinesterase and Butyrylcholinesterase," *RSC Advances* 12 (2022): 19764–19855.

4. R. J. Obaid,. E. U. Mughal, N. Naeem, et al., "Pharmacological Significance of Nitrogen-Containing Five and Six-Membered Heterocyclic Scaffolds as Potent Cholinesterase Inhibitors for Drug Discovery," *Process Biochemistry* 120 (2022): 250–259.

5. A. Blokland, "Acetylcholine: A Neurotransmitter for Learning and Memory?," *Brain Research Reviews* 21 (1995): 285–300.

6. Z. M. Cheema, M. Nisar, H. Y. Gondal, S. A. Alhussain, M. E. A. Zaki, and I. Coldham, "New Benzotriazole-Derived α-Substituted Hemiaminal Ethers With Enhanced Cholinesterase Inhibition Activity: Synthesis, Structural, and Biological Evaluations," *Journal of Saudi Chemical Society* 27 (2023): 101746.

7. R. Chen, X. Li, H. Chen, et al., "Development of the "Hidden" Multi-Target-Directed Ligands by AChE/BuChE for the Treatment of Alzheimer's Disease," *European Journal of Medicinal Chemistry* 251 (2023): 115253.

8. J. Wu, M. Pistolozzi, S. Liu, and W. Tan, "Design, Synthesis and Biological Evaluation of Novel Carbamates as Potential Inhibitors of Acetylcholinesterase and Butyrylcholinesterase," *Bioorganic & Medicinal Chemistry* 28 (2020): 115324.

9. S. Gauthier, P. Rose-Neto, J. A. Morais, and C. Webster, "World Alzheimer Report 2021," accessed December 16, 2024, https://www.alzint.org/u/World-Alzheimer-Report-2021.pdf.

10. L. Jing, W. Wenxiu, B. Meng, et al., "Rapid Discovery and Crystallography Study of Highly Potent and Selective Butylcholinesterase Inhibitors Based on Oxime-Containing Libraries and Conformational Restriction Strategies," *Bioorganic Chemistry* 134 (2023): 106465.

11. A. P. Skaria, "The Economic and Societal Burden of Alzheimer Disease: Managed Care Considerations," *American Journal of Managed Care* 28 (2022): 188–196.

12. Z. R. Chen, J. B. Huang, S. L. Yang, and F. F. Hong, "Role of Cholinergic Signaling in Alzheimer's Disease," *Molecules* 27 (2022): 1816.

13. S. Dhillon, "Aducanumab: First Approval," *Drugs* 81 (2021): 1437–1443.

14. Y. Wang, F. Xu, D. Luo, et al., "Synthesis of Anthranilic Diamide Derivatives Containing Moieties of Trifluoromethylpyridine and Hydrazone as Potential Anti-Viral Agents for Plants," *Journal of Agricultural and Food Chemistry* 67 (2019): 13344–13352.

15. J. Wu, X. Kou, H. Ju, H. Zhang, A. Yang, and R. Shen, "Design, Synthesis and Biological Evaluation of Naringenin Carbamate Derivatives as Potential Multifunctional Agents for the Treatment of Alzheimer's Disease," *Bioorganic & Medicinal Chemistry Letters* 49 (2021): 128316.

16. A. Nerella and M. Jeripothula, "Design, Synthesis and Biological Evaluation of Novel Deoxyvasicinone-Indole as Multi-Target Agents for Alzheimer's Disease," *Bioorganic & Medicinal Chemistry Letters* 49 (2021): 128212.

17. S. Li, A. J. Li, J. Travers, et al., "Identification of Compounds for Butyrylcholinesterase Inhibition," *SLAS Discovery* 26 (2021): 1355–1364.

18. R. B. Teponno, S. R. Noumeur, S. E. Helaly, S. Hüttel, D. Harzallah, and M. Stadler, "Furanones and Anthranilic Acid Derivatives From the Endophytic Fungus *Dendrothyrium variisporum*," *Molecules* 22 (2017): 1674.

19. H. Schrey, F. J. Muller, P. Harz, Z. Rupcic, M. Stadler, and P. Spiteller, "Nematicidal Anthranilic Acid Derivatives From *Laccaria* Species," *Phytochemistry* 160 (2019): 85–91.

20. P. Prasher and M. Sharma, "Medicinal Chemistry of Anthranilic Acid Derivatives: A Mini Review," *Drug Development Research* 82 (2021): 945–958.

21. M. Milusheva, V. Gledacheva, I. Stefanova, et al., "Synthesis, Molecular Docking, and Biological Evaluation of Novel Anthranilic Acid Hybrid and Its Diamides as Antispasmodics," *International Journal of Molecular Sciences* 24 (2023): 13855.

22. A. A. H. M. Eissa, G. A. E. H. Soliman, and M. H. Khataibeh, "Design, Synthesis and Anti-Inflammatory Activity of Structurally Simple Anthranilic Acid Congeners Devoid of Ulcerogenic Side Effects," *Chemical and Pharmaceutical Bulletin* 60 (2021): 1290–1300.

23. G. Oxenkrug, M. Van Der Hart, J. Roeser, and P. Summergrad, "Anthranilic Acid: A Potential Biomarker and Treatment Target for Schizophrenia," *Annals of Psychiatry and Mental Health* 4 (2016): 1059.

24. P. Prasher, M. Sharma, F. Zacconi, et al., "Synthesis and Anticancer Properties of 'Azole' Based Chemotherapeutics as Emerging Chemical Moieties: A Comprehensive Review," *Current Organic Chemistry* 25 (2021): 654–668.

25. P. Marinova and M. Hristov, "Synthesis and Biological Activity of Novel Complexes With Anthranilic Acid and Its Analogues," *Applied Sciences* 13 (2023): 9426.

26. A. Thorarensen, B. D. Wakefield, D. L. Romero, K. R. Marotti, M. T. Sweeney, and G. E. Zurenko, "Preparation of Novel Anthranilic Acids as Antibacterial Agents. Extensive Evaluation of Alternative Amide Bioisosteres Connecting the A- and the B-Rings," *Bioorganic & Medicinal Chemistry Letters* 17 (2007): 2823–2827.

27. A. Kumar, D. Bansal, K. Bajaj, S. Sharma, and V. K. S. Archana, "Synthesis of Some Newer Derivatives of 2-Amino Benzoic Acid as Potent Anti-Inflammatory and Analgesic Agents," *Bioorganic & Medicinal Chemistry* 11 (2003): 5281–5291.

28. K. Chen, Q. Liu, J. P. Ni, H. J. Zhu, Y. F. Li, and Q. Wang, "Synthesis, Insecticidal Activities and Structure–Activity Relationship Studies of Novel Anthranilic Diamides Containing Pyridylpyrazole-4-Carboxamide," *Pest Management Science* 71 (2015): 1503–1512.

29. T. P. Selby, G. P. Lahm, and T. M. Stevenson, "A Retrospective Look at Anthranilic Diamide Insecticides: Discovery and Lead Optimization to Chlorantraniliprole and Cyantraniliprole," *Pest Management Science* 73 (2017): 658–665.

30. E. Teodori, L. Braconi, D. Manetti, M. N. Romanelli, and S. Dei, "The Tetrahydroisoquinoline Scaffold in ABC Transporter Inhibitors That Act as Multidrug Resistance (MDR) Reversers," *Current Topics in Medicinal Chemistry* 22 (2022): 2535–2569.

31. J. W. Zheng and L. Ma, "Metal Complexes of Anthranilic Acid Derivatives: A New Class of Non-Competitive α-Glucosidase Inhibitors," *Chinese Chemical Letters* 27 (2016): 627–630.

32. M. Imran, F. A. Shah, H. Nadeem, et al., "Synthesis and Biological Evaluation of Benzimidazole Derivatives as Potential Neuroprotective Agents in an Ethanol-Induced Rodent Model," *ACS Chemical Neuroscience* 12 (2021): 489–505.

33. Z. Alım, T. Tunç, N. Demirel, A. Günel, and N. Karacan, "Synthesis of Benzimidazole Derivatives Containing Amide Bond and Biological Evaluation as Acetylcholinesterase, Carbonic Anhydrase I and II Inhibitors," *Journal of Molecular Structure* 1268 (2022): 133647.

34. T. Tunç, S. Abdurrahmanoğlu, A. Günel, Z. Alım, and N. Demirel, "Influence of Chirality of Benzimidazole Amine Hybrids on Inhibition of Human Erythrocytes Carbonic Anhydrase I, II and Acetylcholinesterase," *Chemistry and Biodiversity* 20 (2023): e202300207.

35. H. U. Blaser, "Chirality and Its Implications for the Pharmaceutical Industry," *Rendiconti Lincei* 24 (2013): 213–216.

36. S. W. Smith, "Chiral Toxicology: It's the Same Thing…Only Different," *Toxicological Sciences* 110 (2009): 4–30.

37. H. S. Rehan, D. Chopra, and A. K. Kakkar, "Physician's Guide to Pharmacovigilance: Terminology and Causality Assessment," *European Journal of Internal Medicine* 20 (2009): 3–8.

38. W. H. Brooks, W. C. Guida, and K. G. Daniel, "The Significance of Chirality in Drug Design and Development," *Current Topics in Medicinal Chemistry* 11 (2011): 760–770.

39. J. Ceramella, D. Lacopetta, A. Franchini, et al., "A Look at the Importance of Chirality in Drug Activity: Some Significative Examples," *Applied Sciences* 12 (2022): 10909.

40. J. Gal, "Single-Isomer Science: The Phenomenon and Its Terminology," *CNS Spectrums* 7 (2002): 8–13.

41. H. A. McManus and P. J. Guiry, "Coupling of Bulky, Electron-Deficient Partners in Aryl Amination in the Preparation of Tridentate Bis(Oxazoline) Ligands for Asymmetric Catalysis," *Journal of Organic Chemistry* 67 (2002): 8566–8573.

42. J. Escalante, P. P. Flores, and J. M. Priego, "Synthesis of 2,3-Dihydro-4(1*H*)-Quinazolinones," *Heterocycles* 63 (2024): 2019–2032.

43. L. Zhang, Q. Chen, L. Li, et al., "Synthesis of *N*-Unsubstituted and *N*3-Substituted Quinazoline-2,4(1*H*,3*H*)-Diones From *o*-Aminobenzamides and CO_2 at Atmospheric Pressure and Room Temperature," *Organic Letters* 25 (2023): 2471–2475.

44. C. Lamberth, S. Jeanmart, T. Luksch, and A. Plant, "Current Challenges and Trends in the Discovery of Agrochemicals," *Science* 341 (2013): 742–746.

45. G. Q. Lin, Q. D. You, and J. F. Cheng, *Chiral Drugs: Chemistry and Biological Action*, 1st ed. (Wiley, 2011).

46. S. Li, D. Li, T. Xiao, S. Zhang, Z. Song, and H. Ma, "Design, Synthesis, Fungicidal Activity, and Unexpected Docking Model of the First Chiral Boscalid Analogues Containing Oxazolines," *Journal of Agricultural and Food Chemistry* 64 (2016): 8927–8934.

47. Q. Yu, T. E. Baroni , L. Liable-Sands, A. L. Rheingold , and A. S. Borovik, "Synthesis and Structure of Chiral 2,6-Bis[(2-Carbamoylphenyl)Carbamoyl]Pyridine Ligands," *Tetrahedron Letters* 39 (1998): 6831–6834.

48. N. Kausar, S. Muratza, M. A. Raza, et al., "Sulfonamide Hybrid Schiff Bases of Anthranilic Acid: Synthesis, Characterization and Their Biological Potential," *Journal of Molecular Structure* 118 (2019): 8–20.

49. F. S. Tokali, P. Taslimi, N. Sadeghian, T. T. Tok, and I. Gülçin, "Synthesis, Characterization, Bioactivity Impacts of New Anthranilic Acid Hydrazones Containing Aryl Sulfonate Moiety as Fenamate Isosteres," *ChemistrySelect* 8 (2023): e202300241.

50. F. S. Tokalı, P. Taslimi, T. T. Tok, A. Karakuş, N. Sadeghian, and I. Gülçin, "Novel Hydrazones Derived From Anthranilic Acid as Potent Cholinesterases and α-Glycosidase Inhibitors: Synthesis, Characterization, and Biological Effects," *Journal of Biochemical and Molecular Toxicology* 38 (2024): e23521.

51. S. A. Adcock and J. A. McCammon, "Molecular Dynamics: Survey of Methods for Simulating the Activity of Proteins," *Chemical Reviews* 106 (2006): 1589–1615.

52. Z. Wu, J. Shi, J. Chen, D. Hu, and B. Song, "Design, Synthesis, Antibacterial Activity, and Mechanisms of Novel 1,3,4-Thiadiazole Derivatives Containing an Amide Moiety," *Journal of Agricultural and Food Chemistry* 69 (2021): 8660–8670.

53. G. L. Ellman, K. D. Courtney, V. Andres, and R. M. Featherstone, "A New and Rapid Colorimetric Determination of Acetylcholinesterase Activity," *Biochemical Pharmacology* 7 (1961): 88–90.

54. Z. Alım, H. Şirinzade, N. Kılınç, E. Dilek, and S. Süzen, "Assessing Indole Derivative Molecules as Dual Acetylcholinesterase and Butyrylcholinesterase Inhibitors Through In Vitro Inhibition and Molecular Modelling Studies," *Journal of Molecular Structure* 1311 (2024): 138276.

55. M. P. Jacobson, D. L. Pincus, C. S. Rapp, et al., "A Hierarchical Approach to All-Atom Protein Loop Prediction," *Proteins* 55 (2004): 351–367.

56. Schrödinger Release, *Maestro* (Schrödinger, 2024).

57. W. Sherman, T. Day, M. P. Jacobson, R. A. Friesner, and R. Farid, "Novel Procedure for Modeling Ligand/Receptor Induced Fit Effects," *Journal of Medicinal Chemistry* 49 (2006): 534–553.

58. A. Akıncıoğlu, S. Göksu, A. Naderi, H. Akıncıoğlu, N. Kılınç, and I. Gülçin, "Cholinesterases, Carbonic Anhydrase Inhibitory Properties and In Silico Studies of Novel Substituted Benzylamines Derived From Dihydrochalcones," *Computational Biology and Chemistry* 94 (2021): 107565.

59. N. Gök, A. Akıncıoğlu, E. E. Binici, H. Akıncıoğlu, N. Kılınç, and S. Göksu, "Synthesis of Novel Sulfonamides With Anti-Alzheimer and Antioxidant Capacities," *Archiv der Pharmazie* 354 (2021): e2000496.

60. N. Kılınç, M. Açar, S. Tuncay, and Ö. F. Karasakal, "Identification of Potential Inhibitors for Severe Acute Respiratory Syndrome-Related Coronavirus 2 (SARS-CoV-2) Angiotensin-Converting Enzyme 2 and the Main Protease From Anatolian Traditional Plants," *Letters in Drug Design & Discovery* 19 (2022): 996–1006.

61. N. Kılınç, U. Güller, and Z. Alım, "Identification of the Inhibition Effects of Some Natural Antiproliferative Agents on CA-I, CA-II, and AChE Activities Isolated From Human Erythrocytes by Kinetic and Molecular Docking Studies," *Russian Journal of Bioorganic Chemistry* 48 (2022): 720–730.

62. G. M. Sastry, M. Adzhigirey, T. Day, R. Annabhimoju, and W. Sherman, "Protein and Ligand Preparation: Parameters, Protocols, and Influence on Virtual Screening Enrichments," *Journal of Computer-Aided Molecular Design* 27 (2013): 221–234.

63. S. Genheden and U. Ryde, "The MM/PBSA and MM/GBSA Methods to Estimate Ligand-Binding Affinities," *Expert Opinion on Drug Discovery* 10 (2015): 449–461.

Supporting Information

Additional supporting information can be found online in the Supporting Information section.